



## Article

# Use of Concentric Hele-Shaw Cell for the Study of Displacement Flow and Interface Tracking in Primary Cementing

Amir Taheri <sup>1,\*</sup> , Jan David Ytrehus <sup>2</sup>, Bjørnar Lund <sup>2</sup>  and Malin Torsæter <sup>2</sup>

<sup>1</sup> Department of Geoscience and Petroleum, Norwegian University of Science and Technology, S. P. Andersens vei 15A, 7031 Trondheim, Norway

<sup>2</sup> SINTEF Industry, S.P. Andersens vei 15B, 7031 Trondheim, Norway; JanDavid.Ytrehus@sintef.no (J.D.Y.); bjornar.lund@sintef.no (B.L.); Malin.Torsater@sintef.no (M.T.)

\* Correspondence: amir.taheri81@gmail.com

**Abstract:** We present our new designed concentric Hele-Shaw cell geometry with dynamic similarity to a real field wellbore annulus during primary cementing, and then, the results of displacement flow of Newtonian and yield-stress non-Newtonian fluids in it are described. The displacement stability and efficiency, the effect of back, front, and side boundaries on displacement, bypassing pockets of displaced yield-stress fluid in displacing fluid, and the behavior of pressure gradients in the cell are investigated. Applications of intermediate buoyant particles with different sizes and densities intermediate between those of successively pumped fluids for tracking the interface between the two displaced and displacing fluids are examined. The main idea is to upgrade this concentric Hele-Shaw cell geometry later to an eccentric one and check the possibility of tracking the interface between successive fluids pumped in the cell. Successful results help us track the interface between drilling fluid and spacer/cement during primary cementing in wells penetrating a CO<sub>2</sub> storage reservoir and decreasing the risk of CO<sub>2</sub> leakage from them.

**Keywords:** cementing; interface tracking; concentric; Hele-Shaw cell; stable displacement; viscous fingering



**Citation:** Taheri, A.; Ytrehus, J.D.; Lund, B.; Torsæter, M. Use of Concentric Hele-Shaw Cell for the Study of Displacement Flow and Interface Tracking in Primary Cementing. *Energies* **2021**, *14*, 51. <https://dx.doi.org/10.3390/en14010051>

Received: 18 November 2020

Accepted: 20 December 2020

Published: 24 December 2020

**Publisher's Note:** MDPI stays neutral with regard to jurisdictional claims in published maps and institutional affiliations.



**Copyright:** © 2020 by the authors. Licensee MDPI, Basel, Switzerland. This article is an open access article distributed under the terms and conditions of the Creative Commons Attribution (CC BY) license (<https://creativecommons.org/licenses/by/4.0/>).

## 1. Introduction

Primary cementing by the sequential pumping of spacer and cement in wellbore annulus and displacement of the drilling fluid and formation fluids is one of the most crucial operations affecting the integrity of oil and gas wells (Figure 1). The primary cementing operations procedure is pumping non-Newtonian yield-stress fluids of progressively higher density and rheology into the wellbore annulus, spacers with higher density rheology than drilling fluids, and after that cements with higher density and rheology than the other existing fluids in the annulus. This successive pumping is performed to stabilize the displacement process and the interfaces between the fluids in the annulus and to increase displacement efficiency [1,2]. Ideally, all the fluids in the wellbore annulus are displaced evenly, and the cement takes their place without leaving any pockets or channels of mud/spacer along the well. However, several factors cause an imperfect displacement, e.g., an uneven borehole due to soft rocks and washouts and the eccentric positioning of the casing within the borehole, mainly in inclined wellbores. Pockets of non-yielded fluid may be bypassed in such washout sections and narrow parts of an eccentric annulus. Consequently, fluid interfaces in the wellbore annulus generally do not advance uniformly, and the quality of well cementing is decreased. For wells penetrating in CO<sub>2</sub> storage reservoirs, it is essential that all annular cement columns are of high quality. This is due to the buoyancy of CO<sub>2</sub> and because these wells are exposed to harsh conditions, e.g., cooling of the well/formation, elevated pressure, and chemical reactions [3].

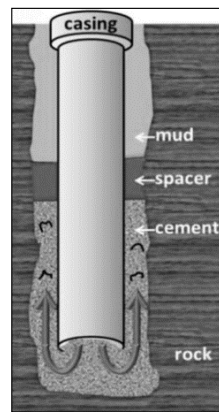


Figure 1. Primary cementing of a well.

There are numerous computational and experimental studies of displacement flow in annular geometries. Due to the problematic rheological behaviors of non-Newtonian fluids, the literature of non-Newtonian displacement flows is less developed than that for Newtonian fluids, especially for experimental studies, and there are fewer experimental studies about displacement flow in concentric and eccentric annular geometries. Mitsuishi and Aoyagi were among the first that studied the relation between pressure drop and flow rate during the displacement flow of non-Newtonian fluids without yield-stress in concentric and eccentric annulus theoretically and experimentally. They observed gravity-driven azimuthal flow (secondary flow) during the displacement flow in the eccentric annulus [4]. Jakobsen et al. experimentally tested the displacement flow of power-law fluids in eccentric annuli and emphasized the importance of fluid viscosity, degree of turbulence, and buoyancy forces on the displacement process [5]. Nouri et al. used Newtonian and non-Newtonian fluids without yield-stress in their concentric and eccentric annuli and measured the mean velocity and corresponding Reynolds shear stresses in a different range of flow with and without rotation of the inner cylinder in their tests [6,7]. Tehrani et al. discussed laminar flow displacement and instability during the flow of Herschel–Bulkley non-Newtonian fluids theoretically and experimentally and by applying dynamic similarity to real field conditions. Their annular experimental setup could be changed from fully concentric to eccentric. They highlighted the importance of the gravity-driven azimuthal flow in eccentric annulus due to the different interface levels of fluids in the wide and narrow sections that causes acceleration of the displacement process but may leave behind an immobile strip of the displaced fluid on the narrow side [8,9]. Escudier et al. presented the distribution of mean velocity and friction factor versus Reynolds number in the flow of non-Newtonian fluid flow in laminar, transitional, and turbulent flow conditions in concentric and eccentric annuli [10,11]. Malekmohammadi et al. confirmed experimentally that several factors such as small eccentricity, increased viscosity/density ratio, and slower flow rates trigger a steady displacement in laminar displacement flows of Newtonian and non-Newtonian fluid with and without yield-stress in vertical narrow eccentric annuli [12]. Kim et al. examined the flow in a concentric annulus with a rotation of the inner cylinder and measured pressure losses and skin friction coefficients for Newtonian and non-Newtonian fluids flows without yield-stress [13]. Ytrehus et al. [14,15] and Sayindla et al. [16] used a large-scale eccentric annular set-up with a test section of 10 m to express the importance of rheological properties of the realistic non-Newtonian fluids for fluid flow and hole cleaning performance extensively.

Another methodology for modeling the annular displacement flow is neglecting the local curvature and unwrapping the annulus into a Hele-Shaw cell (Hele-Shaw slot) [17–20]. This assumption is acceptable when the ratio of the inner radius and the outer radius of the annulus is higher than 0.3 [21]. A Hele-Shaw cell, which consists of two parallel flat plates separated by a defined gap, provides a simple geometry model for experimental and theoretical fluid flow studies. It exploits the mathematical similarity first noted by

Hele-Shaw [22] between slow two-dimensional flows in real geometry and laminar flow in a narrow slot sandwiched between parallel walls. The Hele-Shaw cell has been used extensively in the literature experimentally and theoretically to mimic the vertical section of different geometries such as slender conduits, wellbore annulus, or porous media. One of the main applications of Hele-Shaw cell that has significant practical and scientific importance has been for the study of the viscous fingering instability, mainly using Newtonian fluids [23–29], and also non-Newtonian fluids [30–32]. Bittleston used the Hele-Shaw concept to model an eccentric wellbore annular geometry in their study for more accurate observation of the displacement flows of non-Newtonian fluids in primary cementing of oil and gas wells [17]. Pelipenko and Frigaard studied this model in depth and developed analytical solutions for both concentric and mildly eccentric annuli to study the steady-state displacement during primary cementing and mud removal in an oil well [18–20]. Founar-giotakis et al. presented an approach for the flow of Herschel–Bulkley non-Newtonian fluids in a concentric annulus modeled as a slot in a wide range of flow types and predicted the pressure drop for these conditions [33].

The displacement efficiency and, subsequently, quality of primary well cementing can be evaluated using a cement bond log (CBL) and temperature logs. These logs reveal only large channels in cement and the top of annular cement, and they cannot be used to verify and check the quality of the cement column, e.g., the presence of voids or mud pockets that is required mainly in CO<sub>2</sub> injection wells. Previously, radioactive tracers were used and injected together with cement to specify the top of the annular cement column, but this approach was disregarded considering HSE issues. A recent approach for recognizing the precise location of the interface between successive fluids in a well (e.g., cement-spacer or spacer-mud) is by using tracing particles [34–37]. This includes introducing particles with intermediate buoyancy that remain at the interfaces between successive fluids in a wellbore annulus. These particles must dominate over strong azimuthal secondary flows to move with the interface. Moreover, different fluids can be tracked by dispersing neutrally buoyant particles in the fluids. These particles can be traced using radioactive or electromagnetic tracer devices. This improves the quality of primary cementing of CO<sub>2</sub> wells, where the leakage of CO<sub>2</sub> is a crucial parameter, and CO<sub>2</sub> storage safety would be significantly improved. This methodology has been checked previously by solving the Hele-Shaw model numerically and using the particles in the model. A dimensionless number was also introduced by involving fluids and particle properties and for selecting suitable particles to ensure that the particles can travel toward the interface and move with it [34,35]. Particle motions and interface tracking between fluids were also investigated in different concentric and eccentric annular experimental cells with different fluid rheology and displacement flow rates, and their effectiveness was explored. The experimental results of annular displacement flow of Newtonian/non-Newtonian fluids in eccentric annular cells confirm that particles with a size of 425–500 μm can be useful for tracking the interface between two fluids in cells with a small inclination toward the narrow side, while they are unable to overcome the secondary flows and track the interface in vertical cells [36,37].

Although there have been many studies of the classical Hele-Shaw model for the modeling of displacement flow of non-Newtonian fluids, and to the best of our knowledge, there is no experimental study of displacement flow for the Herschel–Bulkley fluids (that we consider here) in Hele-Shaw cells with dynamic similarity to real concentric and eccentric wellbore annuli. The main objective of this study is to make a Hele-Shaw cell experimental setup that mimics a displacement flow in a “concentric” annulus geometry for checking the feasibility of the use of particles in tracking the interface between two fluids during displacement tests. For this purpose, using different pairs of fully transparent Newtonian and Herschel–Bulkley non-Newtonian fluids and using particles with different properties, several displacement tests are performed in a concentric Hele-Shaw cell geometry. Sensitivity analysis on the fluid properties, flow rate, and particle properties can give us this opportunity to decide about the optimum size and density of the used particle for such applications. Moreover, fingering instabilities in non-Newtonian fluid flow is

investigated here. The concentric Hele-Shaw cell will be upgraded later to an eccentric cell for performing the same tests in it.

## 2. Experimental Description

### 2.1. Experimental Design

To extend the results of displacement experiments to real field practice, we require dynamic similarity with field conditions by providing geometric similarity (aspect ratios) and matching dimensionless parameters governing the flow. This means that together with the aspect ratio of circumferential and radial length scales ( $\delta$ ), experimental Reynolds and Buoyancy numbers that are the main flow-controlling parameters should be close to field values. These numbers are defined as follows:

$$\delta = (r_o - r_i) / \pi(r_o + r_i) \quad (1)$$

$$Re_i = \frac{2\rho_i \bar{w} h}{\mu_{ei}} \quad (2)$$

$$Bu = \frac{\Delta\rho g h^2}{\bar{w} \mu_{e2}} \quad (3)$$

where in these equations, the subscript  $i = 1$  refers to the displaced fluid, and  $i = 2$  indicates the displacing fluid.  $\mu_e$  is an effective viscosity calculated from  $\mu_e = \tau(\gamma_e) / \gamma_e$ , where  $\gamma_e$  is an effective shear rate given by  $\gamma_e = 4\bar{w}/h$ .  $\bar{w}$  and  $h$  are the mean flow velocity and the gap in the annulus, respectively. Typical field values based on cement are reported to be  $\delta = 0.01\text{--}0.1$ ,  $Re_c = 100\text{--}400$ , and  $Bu = 10\text{--}40$  [8,9,12].

Table 1 shows real field data associated with a 16 1/2-inch wellbore with a 13 3/8-inch concentric casing. The length of the cementing section is 500 m, and the annulus has a uniform gap of 0.0397 m. The pump flow rate is 0.02 m<sup>3</sup>/s, and the equivalent mean flow velocity is 0.42 m/s. The calculated Reynolds number and aspect ratio of circumferential and radial length scales ( $\delta$ ) in this real geometry are in the range of the above-reported typical values. The calculated Buoyancy number is not in the reported range but not far from it [5,17].

By down-scaling with a ratio of 0.25 and replacing the density and rheology of the fluids used in the lab (related data to test 7 that will be discussed later) in the calculations, the different parameters and dimensionless numbers of the down-scaled annulus are calculated as recorded in the third column of Table 1. In this down-scaled annular model, the length of the cemented section of the wellbore is one meter, and the aspect ratio of length and width scales ( $\eta = l/h$ ) of 100 were found to be well to produce a fully developed laminar flow, while it is much smaller than a typical value of the real cemented annulus. The aspect ratio of circumferential and radial length scales ( $\delta$ ) is in the range of field values. The dimensionless numbers were calculated by assuming the mean flow velocity of 0.1 m/s, which is a quarter of the field value. While these dimensionless numbers in Table 1 are less than the above-reported field values [8,9], they are in the typical range of existing experimental studies in this area in the literature [12]. We have some limitations for selecting fluid properties for the experiments due to operational difficulties, and the effect of flow velocity on these two dimensionless numbers is on two opposite sides. However, we can decrease the flow velocity to some extent in the performed tests to increase the Buoyancy number. The Reynolds number for the scaled model shows that the displacement flow is fully laminar.

In the down-scaled annular model, the radius ratio is  $r_i/r_o = 0.81 \geq 0.3$ , and it is acceptable to unwrap the annulus into a Hele-Shaw cell. The gap of the Hele-Shaw cell ( $h$ ) representing the constant annular gap is the difference between the outer and inner radii,  $h = (r_o - r_i)$ . The width of the Hele-Shaw cell ( $d$ ) is calculated in such a way to have the same area in the annular and Hele-Shaw cell models,  $d = \pi(r_o + r_i)$ .

The calculated geometries of the Hele-Shaw cell are shown in Table 2, which represents the geometry of the concentric Hele-Shaw cell. This Hele-Shaw cell was intended to mimic



an interval in a wellbore annulus for primary cementing. The main difference between the annular model and the equivalent Hele-Shaw cell is two boundaries in the Hele-Shaw cell. So, for making a Hele-Shaw cell in the lab, we consider twice the calculated width (0.6 m), and we consider a 0.3-m width in the middle section of the model for disregarding the probable boundary effects. The real pump rate in the lab will be  $6 \times 10^{-4} \text{ m}^3/\text{s}$ .

**Table 1.** Real and down-scaled concentric wellbore annulus data [5,8,9,12,17].

Parameters	Real Data	Down-Scaled Data
Length of the Cementing Section ( $l$ ), m	500	1
Wellbore Size, inch	16 1/2	—
Casing Size, inch	13 3/8	—
Wellbore Radius ( $r_o$ ), m	0.2096	0.05274
Casing Radius ( $r_i$ ), m	0.1699	0.04275
Gap ( $h$ ), m	0.0397	0.01
Pump Rate ( $Q$ ), $\text{m}^3/\text{s}$	0.02	$3 \times 10^{-4}$
Mean Flow Velocity ( $\bar{w}$ ), m/s	0.42	0.10
Density of Displaced Fluid ( $\rho_1$ ), $\text{kg}/\text{m}^3$	1440	1000
Density of Displacing Fluid ( $\rho_2$ ), $\text{kg}/\text{m}^3$	1800	1150
Yield-Stress of Displaced Fluid ( $\tau_{y1}$ ), Pa	4.79	0.16
Yield-Stress of Displacing Fluid ( $\tau_{y2}$ ), Pa	7.05	0.39
Consistency Index of Displaced Fluid ( $\kappa_1$ ), $\text{Pas}^n$	0.02	1.29
Consistency Index of Displacing Fluid ( $\kappa_2$ ), $\text{Pas}^n$	0.03	3.43
Flow Behavior Index of Displaced Fluid ( $n_1$ ), dimensionless	0.7	0.5
Flow Behavior Index of Displacing Fluid ( $n_2$ ), dimensionless	1	0.49
Effective Shear Rate ( $\gamma_e$ ), $\text{s}^{-1}$	42.61	40.04
Effective Viscosity of Displaced Fluid ( $\mu_{e1}$ ), Pas	0.1189	0.2078
Effective Viscosity of Displacing Fluid ( $\mu_{e2}$ ), Pas	0.1955	0.5321
Aspect ratio of circumferential and radial length scales ( $\delta$ )	0.033	0.033
Aspect ratio of length and width scales ( $\eta$ )	12598	100
Reynolds Number ( $Re_2$ )	309.05	4.32
Buoyancy Number ( $Bu$ )	67.25	2.76

**Table 2.** Equivalent Hele-Shaw model for concentric annulus.

Length of the Model ( $l$ ), m	Width of the Model ( $d$ ), m	Gap ( $h$ ), m	Pump Rate ( $Q$ ), $\text{m}^3/\text{s}$	Mean Flow Velocity ( $\bar{w}$ ), m/s
1	0.3	0.01	$3 \times 10^{-4}$	0.10

## 2.2. Experimental Set-Up and Procedure

The Hele-Shaw cell consists of two 50 mm thick acrylic plates that stand against each other using a stainless-steel spacer and with a specified and uniform gap of 10 mm. This thickness and material were selected based on deflection calculations and available types to obtain uniform spacing within a defined tolerance. Six inlet and six outlet ports with a diameter of 1/2 inches were drilled into the stainless-steel spacer. For the creation and development of a uniform displacement flow in the cell, a space with a depth of 15 mm, length of 600 mm, and width of 15 mm (more than 10 mm gap in the main body of the cell) were machined in the stainless-steel spacer after the inlet ports and before the outlet ports, as marked by red color in Figure 2b. The pumped fluids are spread in this space before arriving into the cell and flow uniformly through the cell. We have two manifolds before the inlet and after the outlet of the cell for the distribution of the flow from 1-inch pipe into six 1/2-inch inlet and outlet ports of the cell. The dimensions of the Hele-Shaw cell, as mentioned in Table 2, are 60 cm (width)  $\times$  100 cm (height)  $\times$  1 cm (gap). Six 1/4-inch ports at a distance of 10 cm after the inlet were designed to release particles into the cell using six syringes connected to the ports. The drawings of this concentric Hele-Shaw are presented in Figure 2. This cell will be upgraded to an eccentric cell later for further studies.

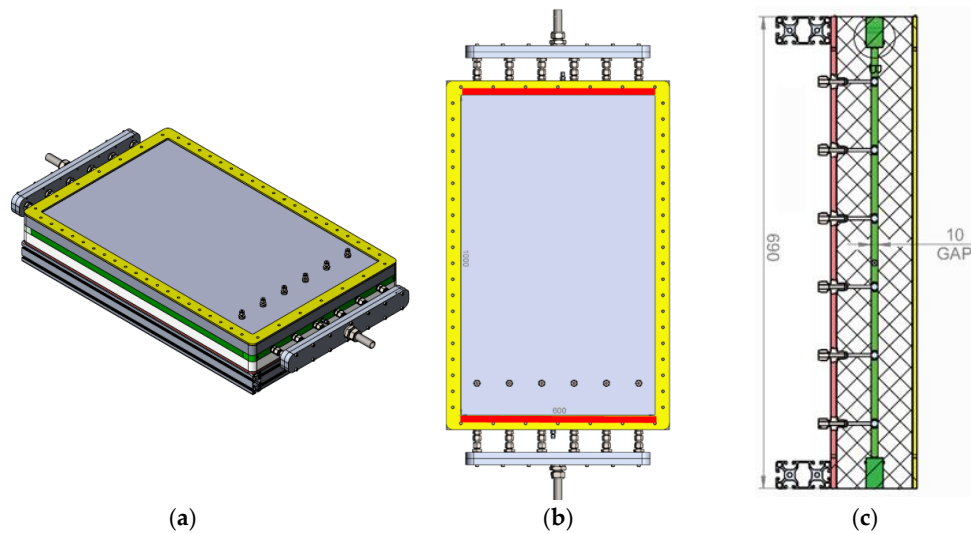


**Figure 2.** Drawing of concentric Hele-Shaw cell. (a) 3D view; (b) Top view; (c) Cross-section view.

The setup of the experiments is shown in Figure 3. Two pumps are used for pumping displacing and displaced fluids in the cell. A constant frequency centrifugal pump is applied for the flow of the displaced fluid, and another one is used for the flow of displacing fluid with a variable frequency drive to adjust the flow rate. A Heinrichs magnetic flow meter with the output signal of 4–20 mA corresponding to 0–150 L/min is utilized to measure the flow rate, and two GE Druck pressure transmitters and a Fuji differential pressure transmitters are applied for measuring the pressure drop over the Hele-Shaw cell. For performing the tests, the cell is in a vertical direction, and flow is in the vertical direction from the bottom to the top. The first step for performing the tests is to initialize the model, obtaining an almost flat and horizontal interface between the displaced and displacing fluids. We have used different approaches to initialize the cell that will be described later. For most experiments, the cell was first filled by a displaced fluid from the bottom. Then, this fluid is displaced with a displacing fluid from the bottom to a specified height with a very small flow rate to have a flat interface between the two fluids at the specified height. For tests with particles, the particles are released into the cell using syringes filled by the particles at different heights relative to the interface. Then, the interface is moved to a height of 20 cm from the entrance slowly (in most cases), and this is the initial status of the interface for the start of the tests. After waiting several minutes for gravity equilibrium in the cell, the experiment starts by pumping the displacing fluid from the bottom into the cell. Flow rate, pressures at the inlet, and outlet and pressure differences are recorded on a PC. Moreover, images of the displacement process are recorded using a Canon EOS 5D Mark IV camera at one-second intervals. A backlight is used for better observation of the displacement process and particles.



**Figure 3.** Experimental setup for performing the tests in the concentric Hele-Shaw cell.

### 2.3. Fluid Preparation and Property Measurement

In this series of experiments, several pairs of Newtonian and non-Newtonian fluids are prepared and used. Water and aqueous sucrose solution are the used Newtonian fluids, and Carbopol-980 solutions at different concentrations are the used non-Newtonian fluid with shear thinning and yield-stress behavior. Carbopol-980 is a white powder used as a thickener, stabilizer, and suspending agent in different industries. The rheological properties of Carbopol solutions are significantly influenced by the Carbopol concentration and the pH of the solution. The yield-stress behavior of a Carbopol solution is achieved at an intermediate pH by neutralizing with a base agent (e.g., NaOH in this study). This neutralized solution is transparent and has the same density as water for low Carbopol concentrations. In preparing the Carbopol solution, we add the Carbopol powder (0.08–0.10 wt/wt %) to water gradually in a mixing tank, and they mix slowly for 3–4 h. We should decrease the mixing rate when adding NaOH to the Carbopol–water solution to prevent introducing air bubbles into the gel-like solution. Brilliant Cresyl Blue, a cationic stable and water-soluble dye, is added to the displaced fluids for visualization purposes [38]. The dye should be added to the Carbopol solutions before NaOH. Rheological measurements showed that a small amount of this dye does not affect the rheology of the fluids. Sucrose and glycerol were used as weighting agents to increase the density of the Carbopol solution, while NaCl was added for increasing the electrical conductivity. Fluid densities and pHs were measured using a DMA-46 densitometer (Anton Paar, Graz, Austria) and pH meter pH 1000 L (VWR International, Radnor, PA, USA), respectively. The rheological properties of the fluids were measured before each test using an Anton Paar MCR 102 rheometer at a fixed temperature of 21 °C. The rheology data were fitted to a Herschel–Bulkley model,  $\tau = \tau_y + \kappa \dot{\gamma}^n$ , where  $n$  is the power-law index,  $\kappa$  is the consistency index, and  $\tau_y$  is the yield-stress. Before data acquisition in the rheometer, a pre-shear of 2 min with a shear rate of  $1000 \text{ s}^{-1}$  is performed on the solutions to reset the structure of the polymers. After pre-shearing, shear stress values were recorded for a decreasing and increasing ramp of shear rates (to check for possible hysteresis) in a logarithmic manner.

Table 3 presents an overview of compositions, pH, and density of the displaced and displacing fluids in the tests.

**Table 3.** Compositions and pHs of the displaced and displacing fluids.

Test	Fluid Type	pH	$\rho$ (g/cc)	Carbopol (wt/wt %)	NaOH (wt/wt %)	Sucrose (wt/wt %)	NaCl (wt/wt %)	Glycerol (wt/wt %)	Blue Dye (wt/wt %)
1	Displaced	—	1.00	0	0	0	0	0	0.000230
	Displacing	—	1.15	0	0	35	0.0325	0	0.000000
2	Displaced	—	1.00	0	0	0	0	0	0.000230
	Displacing	—	1.15	0	0	35	0.0325	0	0.000000
3	Displaced	—	1.00	0	0	0	0	0	0.000230
	Displacing	—	1.15	0	0	35	0.0325	0	0.000000
4	Displaced	—	1.00	0	0	0	0	0	0.000230
	Displacing	—	1.15	0	0	35	0.0325	0	0.000000
5	Displaced	—	1.00	0	0	0	0	0	0.000000
	Displacing	7.40	1.15	0.1	0.035	35	0.0004	0	0.000000
6	Displaced	—	1.00	0	0	0	0	0	0.000230
	Displacing	7.00	1.16	0.1	0.030	0	0.0061	60	0.000000
7	Displaced	7.80	1.00	0.08	0.032	0	0	0	0.000230
	Displacing	7.40	1.15	0.1	0.035	35	0.0004	0	0.000000
8	Displaced	7.80	1.00	0.08	0.032	0	0	0	0.000230
	Displacing	7.40	1.15	0.1	0.035	35	0.0004	0	0.000000
9	Displaced	7.50	1.00	0.1	0.039	0	0	0	0.000230
	Displacing	—	1.15	0	0	35	0.0325	0	0.000000
10	Displaced	7.50	1.00	0.1	0.039	0	0	0	0.000230
	Displacing	—	1.15	0	0	35	0.0325	0	0.000000

Table 3. Cont.

Test	Fluid Type	pH	$\rho$ (g/cc)	Carbopol (wt/wt %)	NaOH (wt/wt %)	Sucrose (wt/wt %)	NaCl (wt/wt %)	Glycerol (wt/wt %)	Blue Dye (wt/wt %)
11	Displaced	8.00	1.00	0.08	0.039	0	0	0	0.000230
	Displacing	—	1.15	0	0	35	0.0325	0	0.000000
12	Displaced	8.00	1.00	0.08	0.039	0	0	0	0.000230
	Displacing	—	1.15	0	0	35	0.0325	0	0.000000
13	Displaced	8.00	1.00	0.08	0.039	0	0	0	0.000230
	Displacing	—	1.15	0	0	35	0.0325	0	0.000000
14	Displaced	8.00	1.00	0.08	0.039	0	0	0	0.000230
	Displacing	—	1.15	0	0	35	0.0325	0	0.000000
15	Displaced	7.10	1.00	0.1	0.032	0	0	0	0.000229
	Displacing	6.50	1.15	0.1	0.032	35	0.0010	0	0.000000
16	Displaced	—	1.14	0	0	35	0	0	0.000150
	Displacing	7.00	1.00	0.1	0.032	0	0.0007	0	0.000000

Table 4 shows the properties of the fluids used in the tests. Subscripts 1 and 2 are representative of displaced and displacing fluids, respectively. The rheology data have been extracted from shear stress vs. shear rate plots shown in the next sections.

Table 4. Density and rheology of the displaced and displacing fluids.

Test	$\rho_1$ (g/cc)	$\rho_2$ (g/cc)	$\tau_{y1}$ (Pa)	$\tau_{y2}$ (Pa)	$\kappa_1$ (Pas <sup>n</sup> )	$\kappa_2$ (Pas <sup>n</sup> )	$n_1$	$n_2$
1	1.00	1.15	0.00	0.00	$9.56 \times 10^{-4}$	$3.17 \times 10^{-3}$	1.00	1.00
2	1.00	1.15	0.00	0.00	$9.56 \times 10^{-4}$	$3.17 \times 10^{-3}$	1.00	1.00
3	1.00	1.15	0.00	0.00	$9.56 \times 10^{-4}$	$3.17 \times 10^{-3}$	1.00	1.00
4	1.00	1.15	0.00	0.00	$9.56 \times 10^{-4}$	$3.17 \times 10^{-3}$	1.00	1.00
5	1.00	1.15	0.00	0.39	$9.56 \times 10^{-4}$	3.43	1.00	0.49
6	1.00	1.16	0.00	0.007	$9.56 \times 10^{-4}$	0.57	1.00	0.72
7	1.00	1.15	0.16	0.39	1.29	3.43	0.50	0.49
8	1.00	1.15	0.16	0.39	1.29	3.43	0.50	0.49
9	1.00	1.15	1.32	0.00	3.50	$3.17 \times 10^{-3}$	0.44	1.00
10	1.00	1.15	1.32	0.00	3.50	$3.17 \times 10^{-3}$	0.44	1.00
11	1.00	1.15	0.26	0.00	1.43	$3.17 \times 10^{-3}$	0.47	1.00
12	1.00	1.15	0.26	0.00	1.43	$3.17 \times 10^{-3}$	0.47	1.00
13	1.00	1.15	0.26	0.00	1.43	$3.17 \times 10^{-3}$	0.47	1.00
14	1.00	1.15	0.26	0.00	1.43	$3.17 \times 10^{-3}$	0.47	1.00
15	1.00	1.15	0.80	0.078	2.99	1.37	0.47	0.50
16	1.14	1.00	0.00	0.23	$3.67 \times 10^{-3}$	1.69	1.00	0.51

Table 5 shows the names and properties of the particles that we have used.

Table 5. Names and properties of the particles.

No.	Particle Name	$d_p$ ( $\mu\text{m}$ )	$\rho_p$ (g/cc)
1	Fluorescent Red Polyethylene Microspheres	425–500	1.086
2	Fluorescent Green Polyethylene Microspheres	710–850	1.025
3	Grey Polyethylene Microspheres	850–1.0	1.05
4	White Polystyrene Polymer Spheres	2960 +/- 50	1.05

#### 2.4. Experimental Overview

Table 6 represents an overview of the performed tests. We have completed sixteen tests in the concentric cell with different pairs of Newtonian and non-Newtonian fluids, particle properties, flow rates, and effective shear rates. In some experiments, we do not use particles, and the objective has been to visualize the displacement and its stability. Different dimensionless numbers have been calculated and reported in this table to compare them

with each other. The calculated dimensionless numbers based on the displacing fluid are  $Re_2 = 0.13$ – $330.84$  and  $Bu = 5.68$ – $2465.84$ . The most similar tests to a real primary cementing operation are tests 7 and 8 with two non-Newtonian fluids with yield-stress behavior, which their Reynolds numbers show a fully laminar flow displacement, and their buoyancy numbers are in the same order of magnitude as the reported values [8,9].

**Table 6.** Overview of the performed tests.

Test	Displaced Fluid	Displacing Fluid	$d_p$ ( $\mu\text{m}$ )	$Q$ (L/min)	$\dot{\gamma}_e$ ( $\text{s}^{-1}$ )	$Re_2$	$Bu$
1	Water	Water + Sugar	500	11.17	12.41	224.92	1520.55
2	Water	Water + Sugar	1000	12.48	13.87	251.30	1360.94
3	Water	Water + Sugar	500	16.01	17.79	322.38	1060.87
4	Water	Water + Sugar	1000	16.43	18.26	330.84	1033.75
5	Water	Carbopol + Sugar	1000	3.71	4.12	0.13	8.29
6	Water	Carbopol + Glycerin	500	11.81	13.12	2.74	17.67
7	Carbopol	Carbopol + Sugar	500	7.86	8.73	0.42	5.68
8	Carbopol	Carbopol + Sugar	N/A	6.46	7.18	0.31	6.23
9	Carbopol	Water + Sugar	N/A	12.02	13.36	242.04	1370.37
10	Carbopol	Water + Sugar	N/A	6.68	7.42	134.51	2465.84
11	Carbopol	Water + Sugar	500	15.46	17.18	311.31	1065.45
12	Carbopol	Water + Sugar	1000	15.17	16.86	305.47	1085.82
13	Carbopol	Water + Sugar	500	11.01	12.23	221.70	1496.08
14	Carbopol	Water + Sugar	1000	7.95	8.83	160.08	2071.93
15	Carbopol	Carbopol + Sugar	N/A	4.23	4.70	0.42	18.92
16	Water + Sugar	Carbopol	N/A	4.31	4.79	0.29	−13.95

### 3. Experimental Results and Discussion

In this section, the snapshots of fluid displacement in the concentric Hele-Shaw cells are presented. The rheological properties of displaced and displacing fluids that have been measured before each test are reviewed and discussed. Moreover, the pressure drop values in each test are described and analyzed. In some experiments, we use particles to see their effectiveness for tracking the interface between the displaced and displacing fluids, and in some of them, the main goal is the observation of displacement and its stability in the Hele-Shaw cells. Minor objectives in performing tests in a concentric Hele-Shaw cell were checking the uniformity of the gap in the cell and the effect of side boundaries on the displacement flow pattern. Moreover, making the right decision about the used displaced and displacing fluids in the eccentric cell has been the next goal. The results are described in two sections; stable displacement tests and unstable displacement tests, and different displacement scenarios are investigated there. Due to limitations in space, a selection of the results is described here.

#### 3.1. Stable Displacement

Gravity and viscous forces play the main role in the stability of displacement, and the fluid density and equivalent viscosity are the key parameters in these two forces. In tests no. 1 to 4, both the displaced and displacing fluids are Newtonian fluids; water and sucrose solution with densities of 1.00 and 1.15 g/cc, and viscosities of  $9.56 \times 10^{-4}$  and  $3.17 \times 10^{-3}$  Pas, respectively. In test no. 5, the Newtonian displaced fluid is water, and the displacing fluid is a Carbopol solution with sucrose as a weighting agent that is a yield-stress non-Newtonian fluid with a density of 1.15 g/cc. In test no. 6, water is considered as a displaced fluid again, but Carbopol solution with glycerin as another weighting agent and a density of 1.16 g/cc is considered as a displacing fluid. The displacing fluid in this test has extremely low yield-stress (0.007 Pa) and high consistency index that cause a power-law behavior with a high equivalent viscosity of the displacing fluid in this test. The rheological behavior and equivalent viscosities of the Newtonian displaced and non-Newtonian displacing fluids in tests no. 5 and 6 are shown in Figure 4, and the effective



shear rate in each test has been marked in the plot of equivalent viscosity. In tests no. 7 and 8, both displaced and displacing fluids are non-Newtonian with yield-stress. The displaced fluid is a Carbopol solution with a density of 1.00 g/cc, and the displacing fluid is a Carbopol+sucrose solution with a density of 1.15 g/cc. Figure 4 shows flow curves and equivalent viscosities of the displaced and displacing fluids in these two tests. In all these tests, the displacing fluids have higher densities and equivalent viscosities than the displaced fluid, and favorable conditions for a stable piston-like displacement with a high efficiency occur, as can be seen in snapshots of the displacement flow in Figures 5–9. The densities of the displaced and displacing fluids in these tests are 1.00 g/cc and 1.15 g/cc, respectively. In tests no. 1 to 4, the viscosity of the displacing fluid is approximately three times the viscosity of the displaced fluid. This ratio is much higher in tests 5 and 6 and lower in tests 7 and 8 with two non-Newtonian fluids. In tests no. 1–7, both displaced and displacing fluids are pumped from the bottom. Due to the non-Newtonian behavior of the fluids in some cases, we should have a very small flow rate for the displacing fluids during initialization to have a flat initial interface between two fluids at the start. This interface in these tests except test no. 6 is placed at the height of 20 cm from the bottom of the cell. The particles are released in the displacing fluid at the height of 10 cm, and they travel toward the interface at the height of 20 cm. In tests no. 5 and 7 and due to the yield-stress behavior of the displacing fluids, released particles are placed at their location without any movement toward the interface, while their density is in between the densities of the displaced and displacing fluids (see Figures 5, 6 and 8 at the time zero). In test no. 6, the initial height of the interface between the two fluids at the time of zero is 10 cm, and particles are released in the displaced fluid with lower viscosity to have them at the interface (see Figure 7 at the time zero). In all cases here, and due to the favorable density and viscosity ratios of the successive pumped fluids, we can see a stable and piston-like displacement, and this stable displacement confirms the existence of a uniform gap in the cell. In tests with a Newtonian displaced fluid (tests no. 1–6), the interface between the two fluids is sharp, while the interface in tests no. 7 and 8 is uneven, as can be seen in Figures 8 and 9. We observe a good tracking of the interface between the two fluids by the particles for all tests with different flow rates and particle sizes. The particle positions in the y-direction (sideways) do not change over time, and they follow the primary vertical flow of the fluids and the interface. Bypassing of pockets of the displaced (blue) yield-stress fluid by the displacing (white) fluid is observed in tests no. 7 and 8, where the displaced fluid is a non-Newtonian fluid with yield-stress (see Figures 8 and 9). In some cases, we have observed particle bonding on the walls. The side boundary effects have been negligible in these tests.

In test no. 8, the cell was first filled by the white fluid from the bottom for initialization, and then this fluid is displaced by the blue fluid from the top to reach the interface to the height of 20 cm from the bottom. In this case, the front and back walls above the interface and in contact with the displaced (blue) fluid have been wetted by the displacing (white) fluid. Figure 9 shows that we have a stable and piston-like displacement in this test by the start of the flow and advancing the time. By comparing these snapshots with the snapshots of displacement flow in test no. 7 in Figure 8 with the same fluids and almost the same flow conditions, it can be concluded that the wall wetting does not affect stable displacement in these tests. We have observed bypassing the pockets of the white fluid in the blue fluid during initialization in this test, while it seems that the wetting of the walls by the displacing fluid affects the trapping of the displaced fluid below the interface. The trapping of the pockets of the displaced fluid by the displacing fluid during the main displacement has been decreased in comparison to test no. 7. Trapping of the pockets of one fluid in another one can cause some defects in primary cementing jobs.

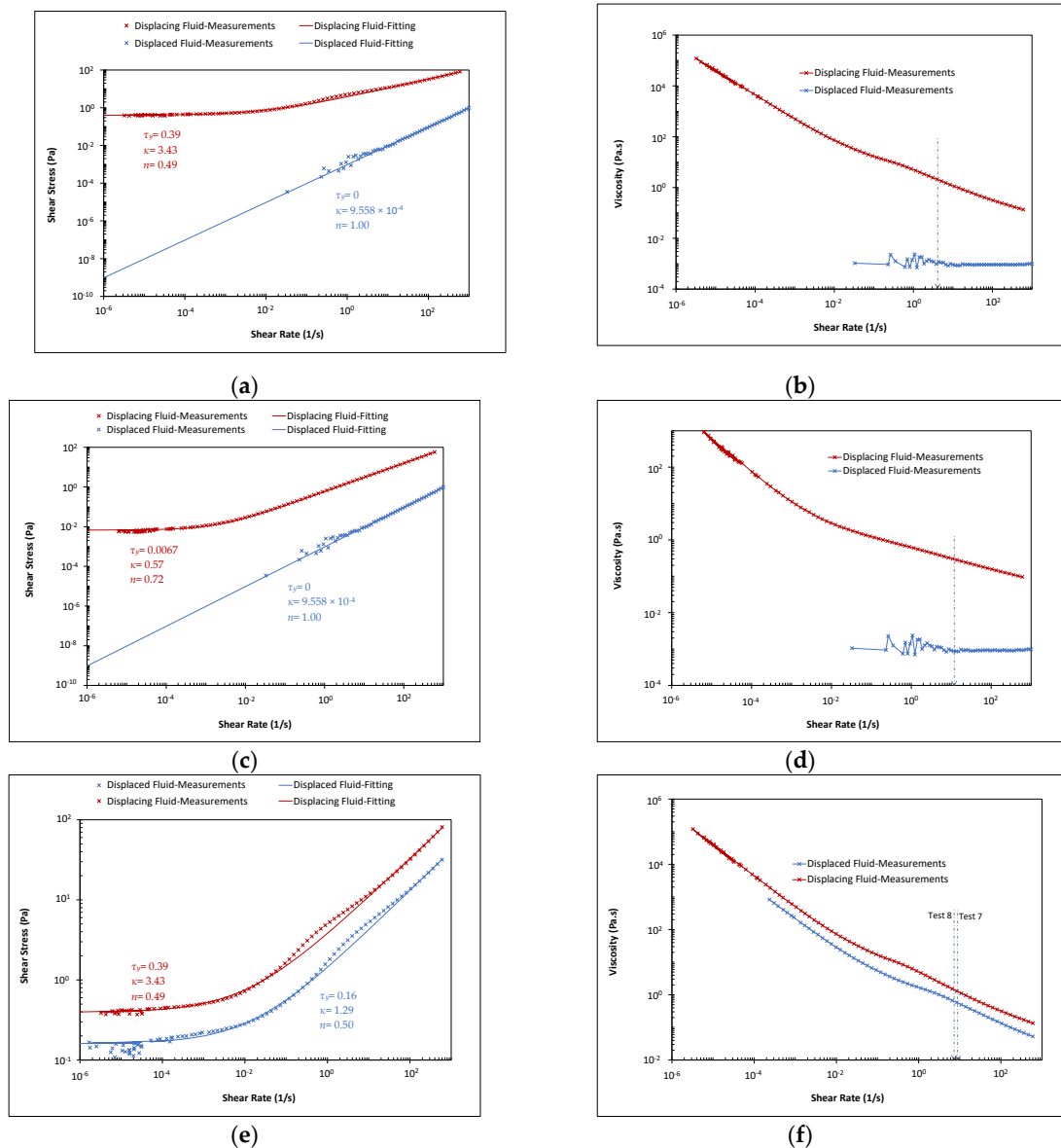


**Figure 4.** Flow curves and equivalent viscosities of the fluids in tests no. 5 to 8. (a) Flow curve in test 5; (b) Equivalent viscosity in test no. 5; (c) Flow curve in test no. 6; (d) Equivalent viscosity in test no. 6; (e) Flow curve in tests no. 7 and 8; (f) Equivalent viscosity in tests no. 7 and 8.

The pressure gradients recorded by the two GE Druck pressure transmitters are plotted for four of the stable displacement tests and are compared in Figure 10a.  $\Delta P$  is the measured pressure drop in the cell, and  $L$  is the height of the cell in this plot. The x-axis is the volume of the pumped displacing fluid. The measured pressure gradient involves hydrostatic and frictional pressure drops. The hydrostatic pressure drop, which is the dominant pressure drop, varies over time due to changing the volume of existing displaced and displacing fluids with different fluid densities in the cell. The main determinants in frictional pressure drop are fluid velocities in the cell and fluid viscosity. Figure 10a shows that an increasing trend exists in the measured pressure gradient in all four tests for the whole period of the displacement. Test no. 4 with two Newtonian fluids has the lowest pressure gradient, and test no. 7 with two non-Newtonian fluids with yield-stress has the highest pressure gradient. Tests no. 5 and 6 with a Newtonian displaced fluid and a non-Newtonian displacing fluid are in the middle. In test no. 5, the displacing fluid is a non-Newtonian fluid with yield-stress, and in test no. 6, the displacing fluid is a power-law fluid with lower equivalent viscosity than the displacing fluid in test no. 5. The different

viscosities of the displaced and displacing fluids in stable displacement tests cause different frictional pressure drops in these cases, while the hydrostatic pressure drop is equal for all tests with the same volume of the fluids in the cell. Tests no. 1 to 4 have almost the same pressure gradient, and the change in the flow rate does not affect the pressure gradient due to a negligible portion of the frictional pressure drop in these four tests with two Newtonian fluids with low equivalent viscosities. So, the pressure gradient of test no. 4 in Figure 10a is the hydrostatic pressure gradient for all tests, and the difference between the pressure gradients of the other tests and test no. 4 represents the frictional pressure gradient in the other tests. Figure 10b shows the calculated frictional pressure gradients for tests no. 5, 6, and 7, indicating increasing trends in frictional pressure gradients in these stable displacement tests over time. In test no. 7 with two non-Newtonian fluids, the frictional pressure gradient is more significant than the tests with one or two Newtonian fluids due to the higher equivalent viscosities of the fluids. Test no. 6 has the lowest frictional pressure gradients due to the lowest equivalent viscosity of the displacing fluid (see Figure 4), while it has a higher flow rate than test no. 5. At the start of the tests, the measured pressure gradients and the calculated frictional pressure gradients have strange behavior due to the initial disturbances and unstable conditions.

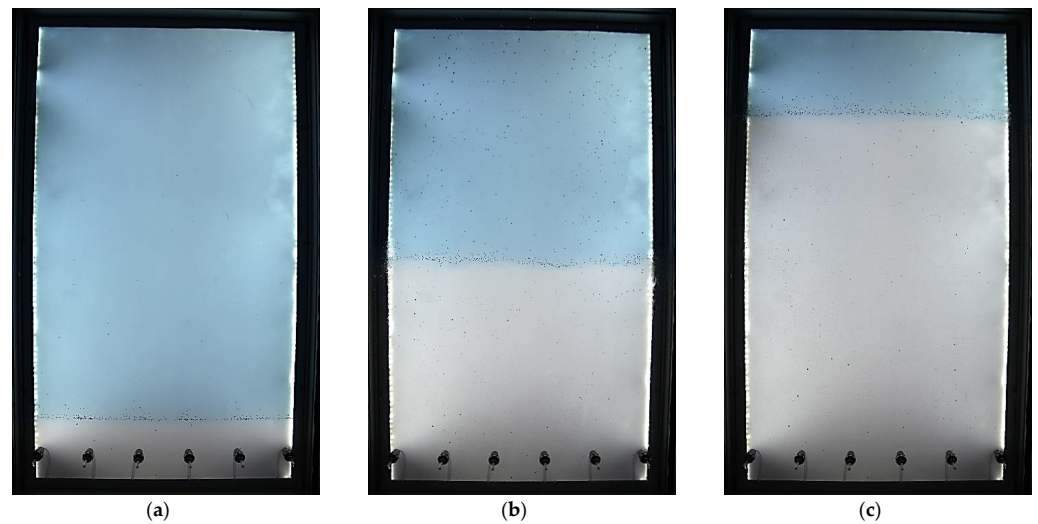


Figure 5. Snapshots of displacement flow in test no. 4. (a)  $t = 0$  s; (b)  $t = 6$  s; (c)  $t = 12$  s.

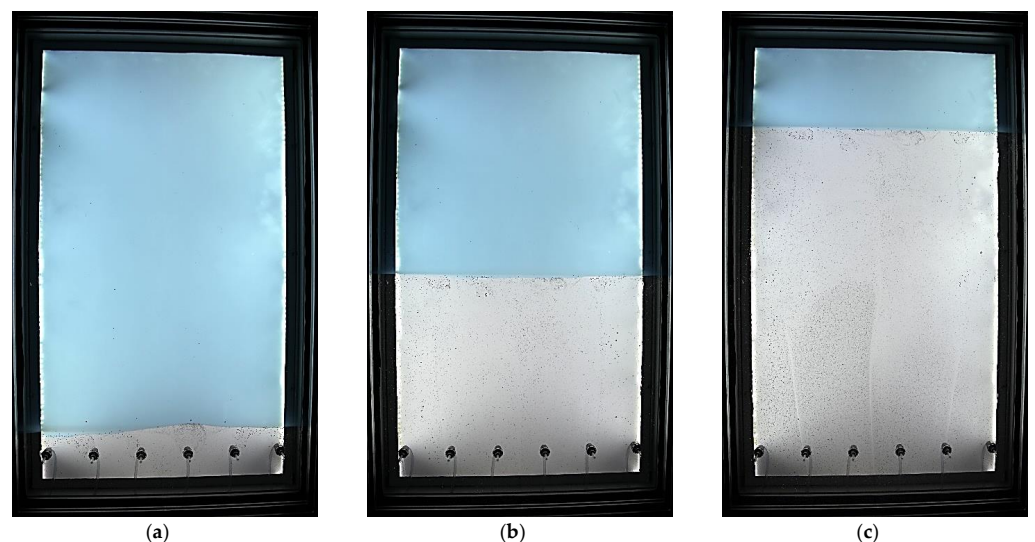


Figure 6. Snapshots of displacement flow in test no. 5. (a)  $t = 0$  s; (b)  $t = 31$  s; (c)  $t = 62$  s.

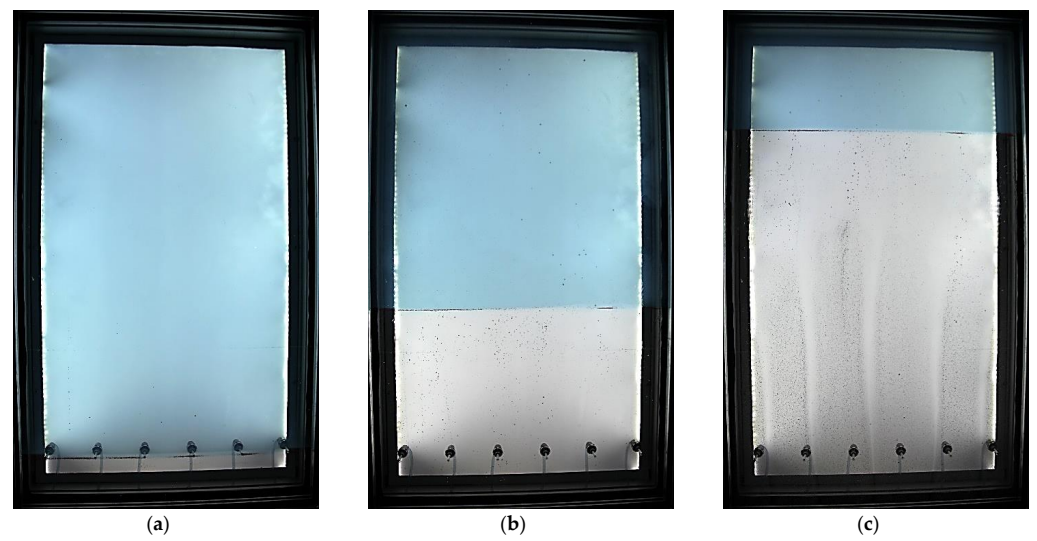


Figure 7. Snapshots of displacement flow in test no. 6. (a)  $t = 0$  s; (b)  $t = 10$  s; (c)  $t = 20$  s.

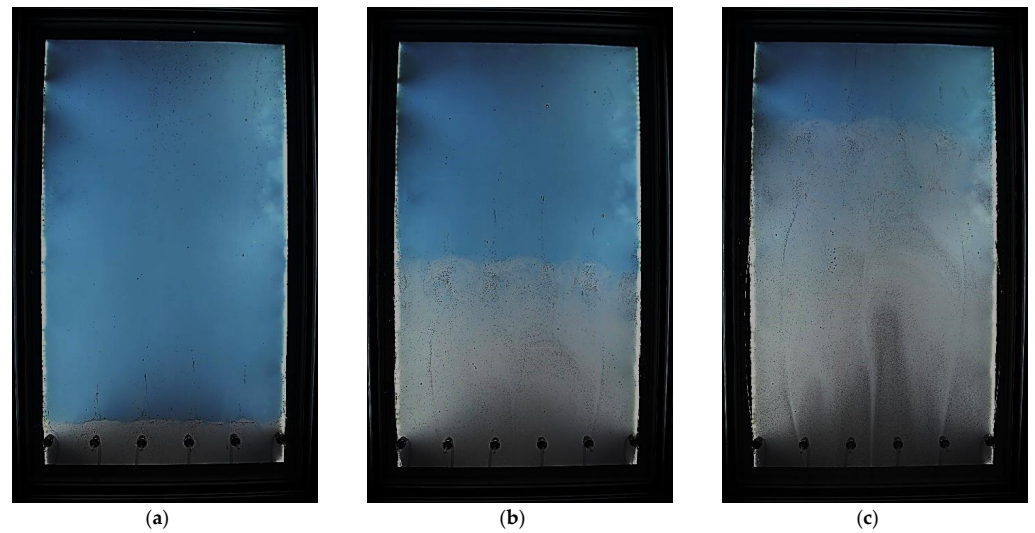


Figure 8. Snapshots of displacement flow in test no. 7. (a)  $t = 0$  s; (b)  $t = 12$  s; (c)  $t = 23$  s.

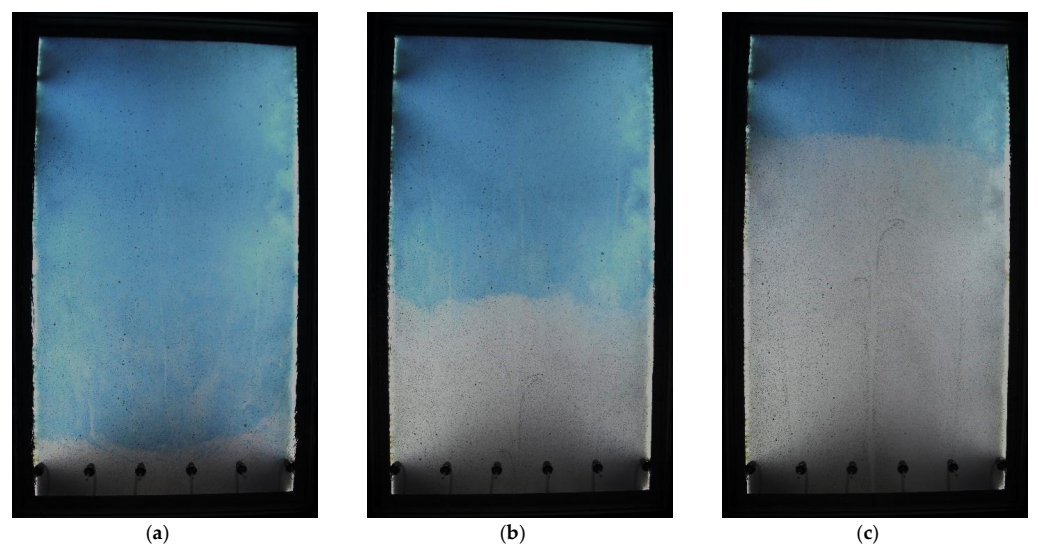
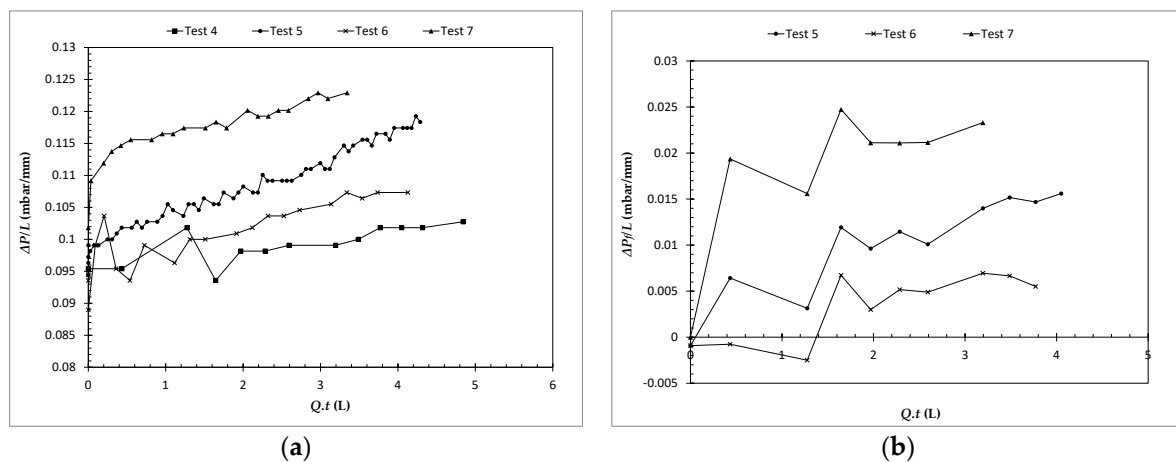


Figure 9. Snapshots of displacement flow in test no. 8. (a)  $t = 0$  s; (b)  $t = 13$  s; (c)  $t = 26$  s.





**Figure 10.** Pressure gradients in stable displacement tests. (a) Total pressure gradients; (b) frictional pressure gradients.

### 3.2. Unstable Displacement

In cases where the density and/or equivalent viscosity of the displacing fluid are lower than the displaced fluid, favorable conditions for a stable displacement vanish. Different kinds of unstable and poor efficient displacements happen in these conditions depending on the fluid and flow properties.

In tests no. 9 and 10, a non-Newtonian Carbopol solution with a density of 1.00 g/cc and a Newtonian sucrose solution with a density of 1.15 g/cc are considered as displaced and displacing fluids, respectively. The pumping flow rate in test no. 9 is twice the flow rate in test no. 10. From Figure 11, which compares the flow curves and equivalent viscosities of the displaced and displacing fluids in these two tests, it can be seen that the displaced fluids are non-Newtonian fluids with yield-stress, and their equivalent viscosities at the marked shear rates are significantly higher than the constant viscosity of the Newtonian displacing fluids. Thus, the displacing fluids have a higher density but lower equivalent viscosity than the displaced fluids. Figures 12 and 13 show snapshots of displacement flow in these two tests. In test no. 9, both displaced and displacing fluids are pumped from the bottom of the cell to initialize the cell. Snapshots of displacement flow show a non-flat initial interface before the start of the test and unstable and poor displacement because of a strong viscous fingering due to the low viscosity of the displacing fluid. The pattern of this strong viscous fingering is also related to the shape of the interface between the two fluids at the time zero. In test no. 10, and for achieving a flat initial interface between the two fluids at the start, the cell is first filled with the white fluid from the bottom. Then, this fluid is displaced toward the bottom of the cell with the pumping of the blue fluid from the top with lower density and higher viscosity than the white fluid to have stable displacement. This initialization approach causes a flatter initial interface between the two fluids at the time zero, as can be seen in Figure 13 at the time of zero. It should be considered that the back and front walls above the interface are wetted with the white fluid in this approach for the initialization. By the start of displacement and advancing the time in test no. 10, we can see unstable and poor displacement due to a weak viscous fingering. The main reasons for this weaker viscous fingering in test no. 10 than test no. 9 is the lower displacement flow rate in this test. Moreover, the flatter initial interface between the two fluids at the time zero and the wetting of the walls above the interface by the displacing fluid in test no. 10 can affect viscous fingering that should be investigated more. Bypassing of pockets of yield-stress displaced fluid by the displacing Newtonian fluid is observed, and this bypassing is increased by increasing the viscous fingering.



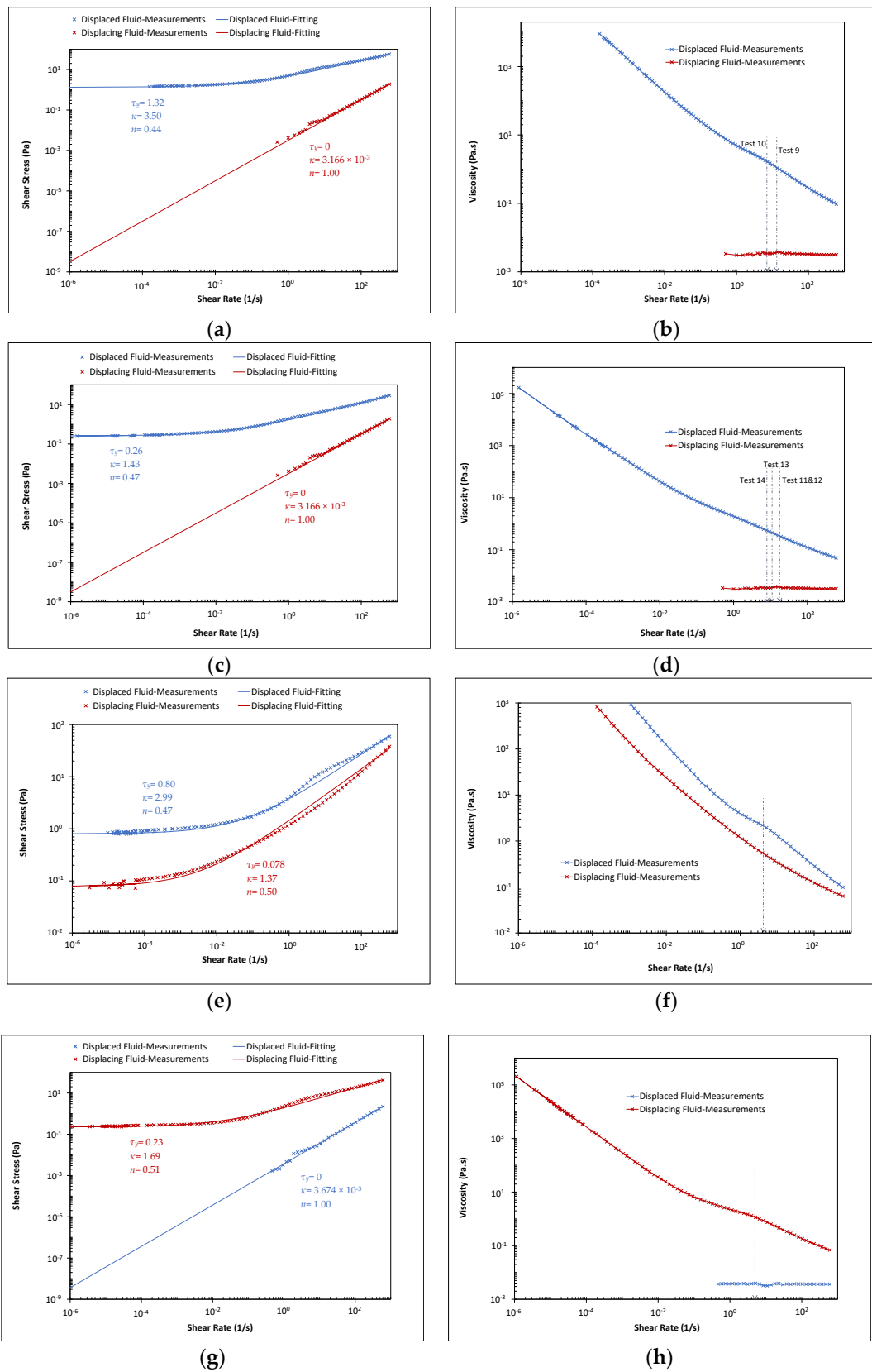


**Figure 11.** Flow curves and equivalent viscosities of the fluids in tests no. 9 to 16. (a) Flow curve in tests no. 9 and 10; (b) Equivalent viscosity in tests 9 and 10; (c) Flow curve in tests no. 11 to 14; (d) Equivalent viscosity in tests no. 11 to 14; (e) Flow curve in test no. 15; (f) Equivalent viscosity in test no. 15; (g) Flow curve in test no. 16; (h) Equivalent viscosity in test no. 16.

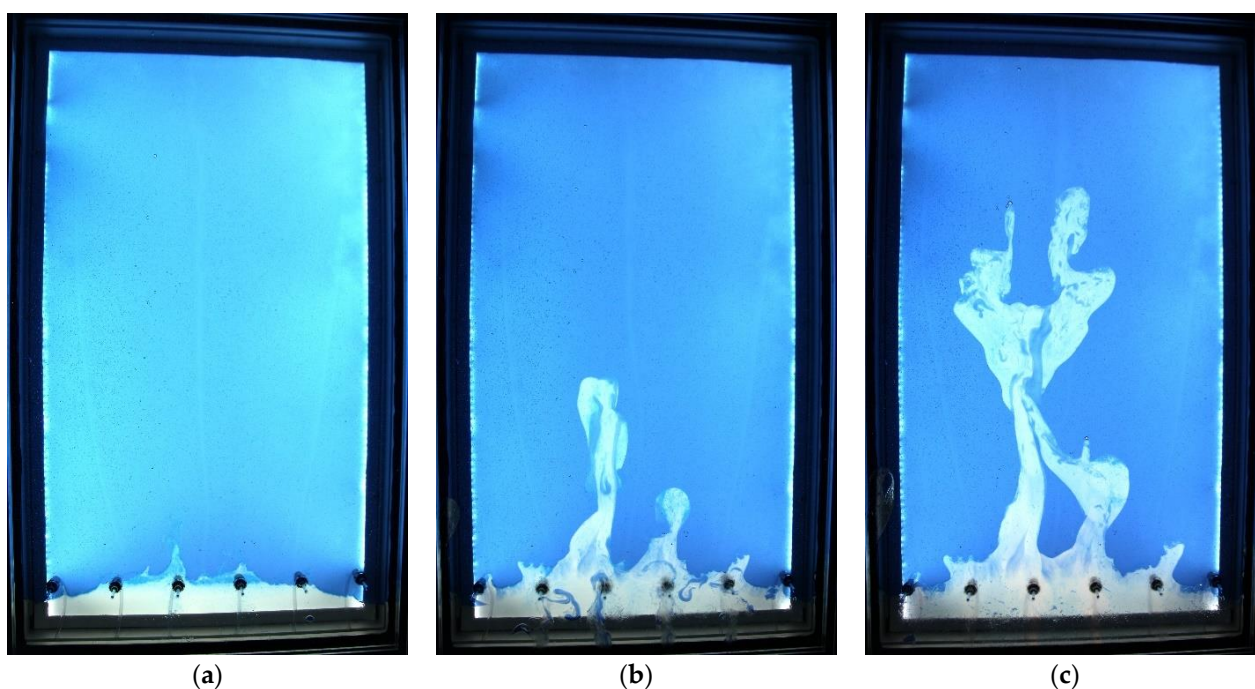


**Figure 12.** Snapshots of displacement flow in test no. 9. (a)  $t = 0$  s; (b)  $t = 4$  s; (c)  $t = 7$  s.

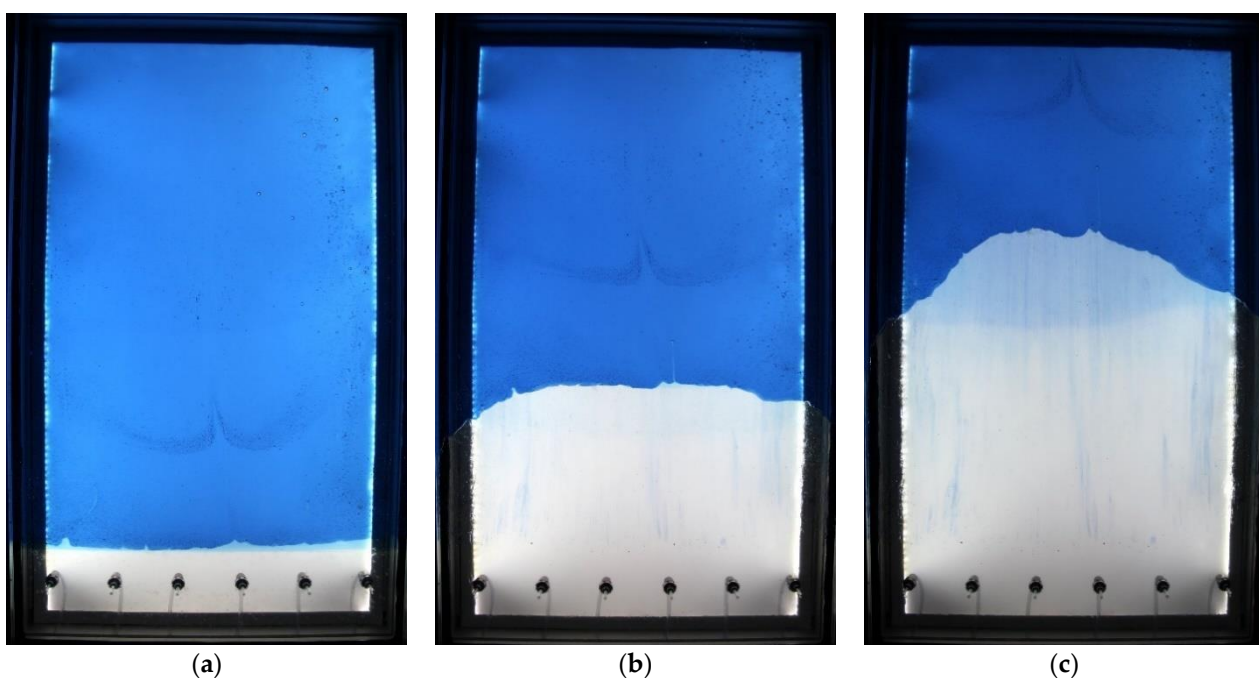


**Figure 13.** Snapshots of displacement flow in test no. 10. (a)  $t = 0$  s; (b)  $t = 11$  s; (c)  $t = 22$  s.

In tests no. 11 to 14, the displaced fluid is a Carbopol solution with a density of 1.00 g/cc, and the displacing fluid is a sucrose solution with a density of 1.15 g/cc. From Figure 11, the displaced fluid is a non-Newtonian fluid with yield-stress, and the displacing fluid is a Newtonian fluid with a lower equivalent viscosity than the displaced fluid. The displaced fluids in these tests have a lower concentration of Carbopol and thus lower yield-stress and equivalent viscosity than the displaced fluids in tests no. 9 and 10. In these four tests, and for a flatter initial interface between the two fluids at the start, we have pumped blue fluid from the top and white fluid from the bottom (similar to test no. 10). It causes almost a flat interface between the two fluids before the displacement, as can be seen

in Figures 14 and 15. Similar to the previous two tests, the displacing fluid has a lower equivalent viscosity and higher density than the displaced fluid, which causes unstable displacement and weak viscous fingering for these test with a flow rate range of 15.46 to 7.95 L/min, as can be seen in snapshots of displacement flow in Figures 14 and 15. As can be seen in these two tests and in Figures 13 and 14, a higher flow rate of 15.17 L/min in test no. 12 results in stronger viscous fingering than the test no. 14 with a flow rate of 7.95 L/min. Similar to previous tests, bypassing pockets of yield-stress displaced fluid by the displacing Newtonian fluid is observed in all tests, and this bypassing increases by increasing the displacement flow rate. In these four tests, particles with different sizes are released in the displacing fluid, and then they travel to the interface between the two fluids and are immersed on the interface at the height of 20 cm from the bottom of the cell. We can see proper tracking of the interface between the fluids by the particles. Moreover, we can see that the particles can track the interface between the fluids in the fingers. Particle bonding on the wall is observed in some cases, and the effect of side boundaries is not significant.

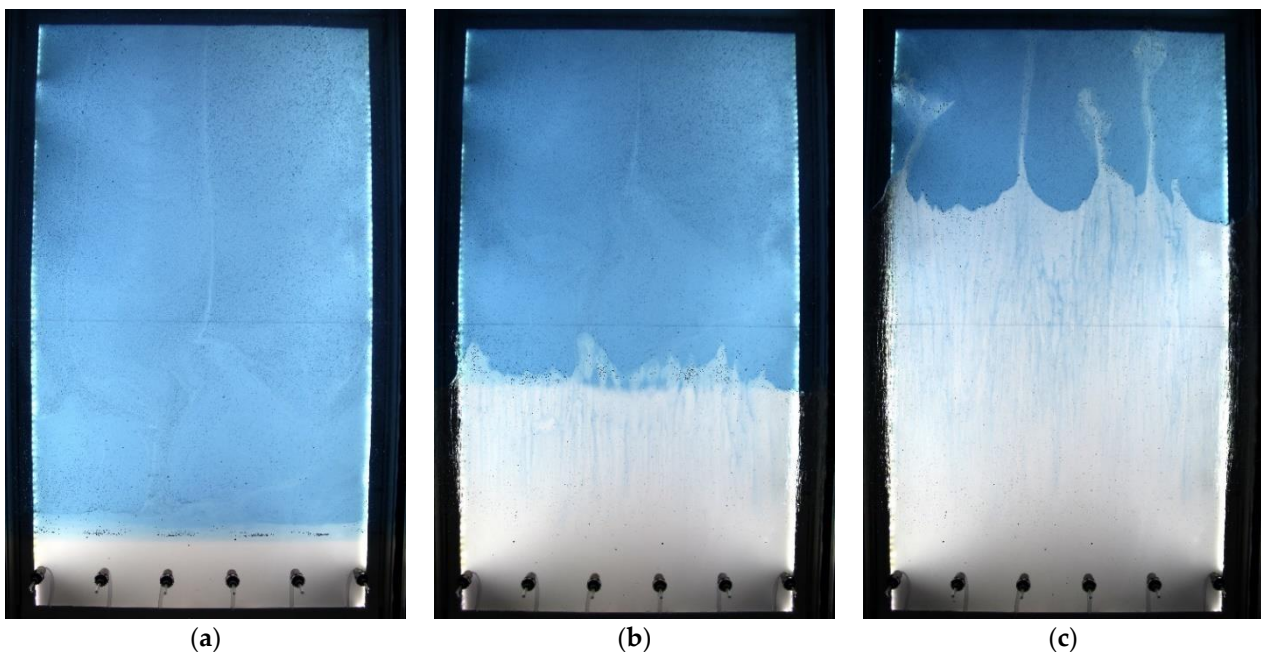


**Figure 14.** Snapshots of displacement flow in test no. 12. (a)  $t = 0$  s; (b)  $t = 5$  s; (c)  $t = 10$  s.

In test no. 15, displaced fluid is a Carbopol solution with a density of 1.00 g/cc, and displacing fluid is a Carbopol+sucrose solution with a density of 1.15 g/cc. Figure 11 shows that both fluids have non-Newtonian behavior with a yield-stress, and the displaced fluid has a higher equivalent viscosity than the displacing fluid. The addition of sucrose to a Carbopol solution causes a decrease in the yield-stress and equivalent viscosity. By applying the same initialization procedure as the previous tests in this section for having an initial flat interface between the two fluids at the time zero, we observe an almost stable and piston-like displacement at the start, and then small deformation of the interface is observed. It may later develop into fingers due to the equivalent viscosities of the fluids in this test. In this test, the displacing fluid has a higher density and lower viscosity than the displaced fluid, but the differences between the equivalent viscosities of the two fluids are smaller than the previous tests. Moreover, the displacement flow rate in this test is 4.23 L/min, which is lower than the previous tests, and all result in an interface deformation and weak viscous fingering later, as shown in Figure 16.

In test no. 16, sucrose solution with a density of 1.14 g/cc and Carbopol solution with a density of 1.00 g/cc are considered as displaced and displacing fluids, respectively. The displaced fluid is a Newtonian fluid, and the displacing fluid is a non-Newtonian fluid



with yield-stress, as can be seen in Figure 11. For the initialization of the cell, we pump both fluids from the bottom of the cell. In this test, the displacing fluid has a lower density and higher equivalent viscosity than the displaced fluid, which causes extremely poor displacement efficiency due to bubble flow displacement, as can be seen in the snapshots of displacement in Figure 17. Drops of the displacing fluid move toward the top of the cell in the displaced fluid due to their lower density, and the displaced blue fluid remains in the cell.

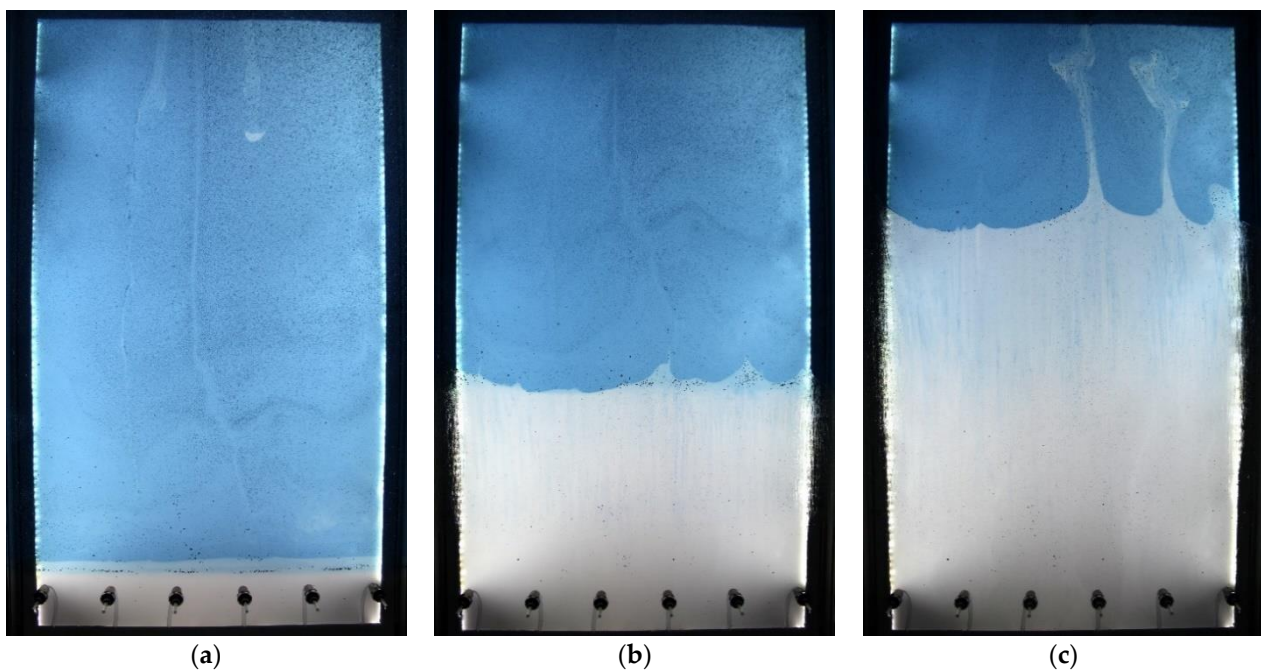


Figure 15. Snapshots of displacement flow in test no. 14. (a)  $t = 0$  s; (b)  $t = 9$  s; (c)  $t = 18$  s.

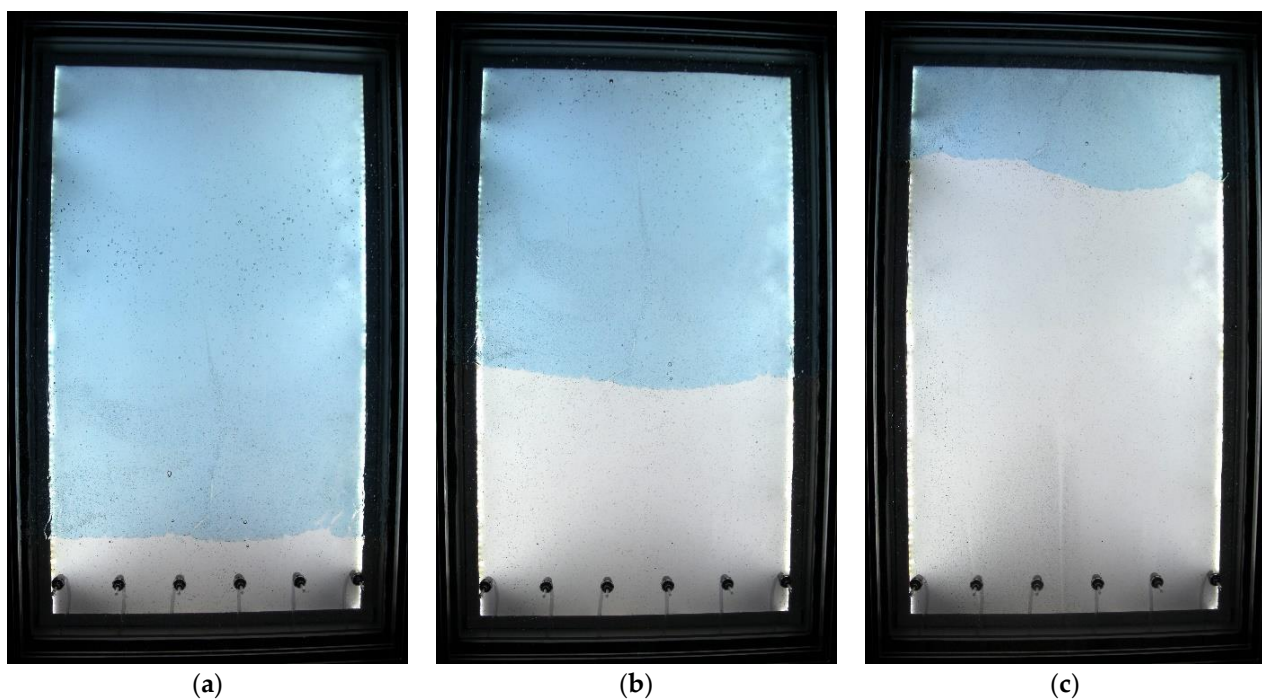


Figure 16. Snapshots of displacement flow in test no. 15. (a)  $t = 0$  s; (b)  $t = 22$  s; (c)  $t = 46$  s.

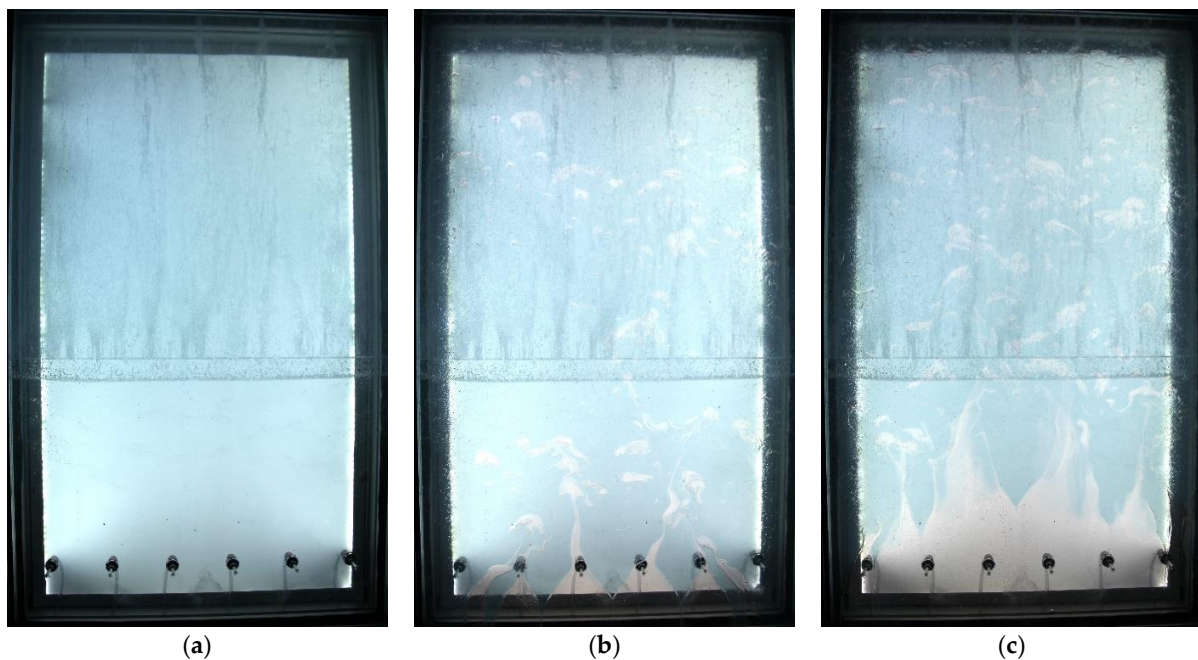


Figure 17. Snapshots of displacement flow in test no. 16. (a)  $t = 0$  s; (b)  $t = 32$  s; (c)  $t = 65$  s.

Figure 18a shows the measured pressure gradients in the tests with unstable displacement. Only the pressure gradients in tests 10, 12, 14, and 16 are displayed here. In tests with viscous fingering (tests 9 to 15), after abnormal pressure behaviors due to the start of the tests and initial disturbances, the pressure gradients increase over time in all cases. Then, constant pressure gradients are observed because of the viscous fingering. Tests 11 to 14 have lower pressure gradients than tests 9 and 10 due to the lower equivalent viscosity of the displaced fluid in these tests. The higher flow rate in test no. 12 causes a higher pressure gradient in this test than in test no. 14 with the same fluids. In test no. 16 with bubble flow, when a displacing fluid has a lower density than the displaced fluid, a constant pressure gradient is observed in the whole period of the test. The calculated frictional pressure gradients in tests no. 10, 12, and 14 are shown in Figure 18b for times before the breakthrough of the displacing fluids (or fingers) to the top boundary of the cell. After increasing the frictional pressure gradients, decreasing trends are observed in tests no. 10 and 14 over time and when the viscous fingering is dominating. In test no. 12, this trend is nearly constant, and it seems that the test duration is not enough to see the dominating effects of viscous fingering in frictional pressure data.

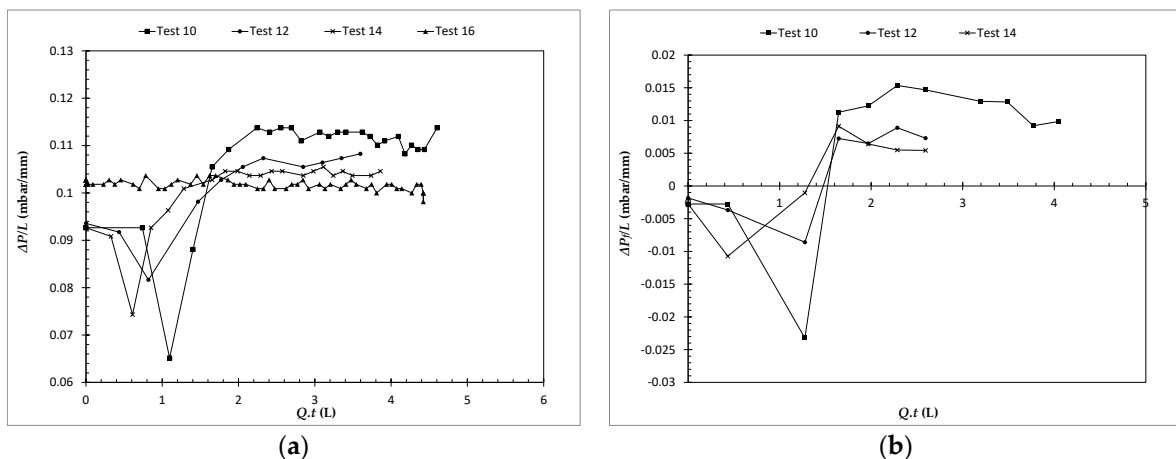


Figure 18. Pressure gradients in unstable displacement tests. (a) Total pressure gradients; (b) frictional pressure gradients.



#### 4. Conclusions

In this study, different displacement scenarios were performed in a concentric Hele-Shaw cell geometry with dynamic similarity to a real field wellbore annulus during primary cementing and by using different pairs of Newtonian and yield-stress non-Newtonian fluids. Displacement pattern and efficiency, pressure gradient behavior, and the performance of tracing particles with intermediate density on the interface between the displaced and displacing fluids were investigated.

1. Our qualitative results confirm that while the vertical displacement of a fluid by another with higher density and viscosity is stable with a flat interface, the displacement of a fluid with another one with lower equivalent viscosity causes viscous fingering and unstable displacement. Viscous fingering increases by increasing the displacement flow rate and the difference of equivalent viscosities of the two fluids. Moreover, displacement of a fluid with another one with lower density causes bubble flow and extremely poor displacement.
2. Bypassing of pockets of the displaced yield-stress fluid by the displacing fluid has been another observed phenomenon in the experiments. This bypassing has also been observed in stable displacement cases and increases by decreasing displacement efficiency and increasing viscous fingering. Displacement of a yield-stress fluid by another yield-stress fluid decreases the bypassing of the pockets of yield-stress displaced fluid, and its possibility is decreased when the two fluids have close yield-stresses.
3. While measured pressure gradients show an increasing trend for the whole period of the tests in the stable displacement tests, they initially increase in all unstable displacement cases and then become constant and continue due to the viscous fingering. The calculated frictional pressure gradients show increasing trends for stable displacement tests and increasing trends followed by decreasing trends for unstable displacement tests. A constant pressure gradient is observed in the whole period of the test with the bubble flow.
4. In all cases consisting of stable and unstable displacements, proper tracking of the interface and fingers by the particles were observed. Tracing particles with different sizes and with intermediate densities on the interface always track the interface and move by it.
5. Wetting of displaced fluid wall with the displacing fluid and changing the properties of front and back boundaries and the existence of side boundaries have no significant effect on the displacement pattern and efficiency.

**Author Contributions:** Conceptualization, J.D.Y. and M.T.; methodology, A.T. and B.L.; validation, A.T., B.L. and J.D.Y.; formal analysis, A.T. and B.L.; investigation, A.T., B.L. and J.D.Y.; writing—original draft preparation, A.T.; writing—review and editing, A.T., B.L. and J.D.Y.; visualization, A.T.; supervision, J.D.Y. and M.T.; project administration, J.D.Y. and M.T.; funding acquisition, J.D.Y. and M.T. All authors have read and agreed to the published version of the manuscript.

**Funding:** This report has been produced in the project “Studying moving fluid interfaces during cementing of CCS wells” funded by the Research Council of Norway (268510/E20).

**Institutional Review Board Statement:** Not applicable.

**Informed Consent Statement:** Not applicable.

**Data Availability Statement:** No new data were created or analyzed in this study. Data sharing is not applicable to this article.

**Acknowledgments:** The authors would like to thank the Research Council of Norway for funding this work. The authors also thank Ali Taghipour and Martin Røphaug from SINTEF Industry for providing laboratory equipment and instrumentation. The support from Alexandre Lavrov from NTNU for designing the experiments and discussions is highly appreciated.

**Conflicts of Interest:** The authors declare no conflict of interest.

## References

1. Nelson, E.B.; Guillot, D. *Well Cementing*; Schlumberger: Houston, TX, USA, 2006.
2. Bishop, M.; Moran, L.; Stephens, M.; Reneau, W. A robust, field friendly, cement spacer system. In Proceedings of the AADE Fluids Conference and Exhibition, Houston, TX, USA, 8–9 April 2008; AADE-08-DF-HO-07.
3. Lavrov, A.; Torsæter, M. *Physics and Mechanics of Primary Well Cementing*; Springer: Berlin/Heidelberg, Germany, 2016.
4. Mitsuishi, N.; Aoyagi, Y. Non-newtonian fluid flow in an eccentric annulus. *J. Chem. Eng. Jpn.* **1973**, *6*, 402–408. [[CrossRef](#)]
5. Jakobsen, J.; Sterri, N.; Saasen, A.; Aas, B.; Kjosnes, I.; Vigen, A. Displacements in eccentric annuli during primary cementing in deviated wells. In Proceedings of the SPE Production Operations Symposium, Oklahoma City, OK, USA, 7–9 April 1991; SPE Paper no. 21686.
6. Nouri, J.M.; Umur, H.; Whitelaw, J.H. Flow of Newtonian and non-Newtonian fluids in concentric and eccentric annuli. *J. Fluid Mech.* **1993**, *253*, 617–641. [[CrossRef](#)]
7. Nouri, J.M.; Whitelaw, J.H. Flow of Newtonian and non-Newtonian fluids in an eccentric annulus with rotation of the inner cylinder. *Int. J. Heat Fluid Flow* **1997**, *18*, 236–246. [[CrossRef](#)]
8. Tehrani, A.; Ferguson, J.; Bittleston, S. Laminar displacement in annuli: A combined experimental and theoretical study. In Proceedings of the SPE Annual Technical Conference and Exhibition, Washington, DC, USA, 4–7 October 1992; SPE-24569-MS.
9. Tehrani, A.; Bittleston, S.H.; Long, P.J.G. Flow instabilities during annular displacement of one non-Newtonian fluid by another. *Exp. Fluids* **1993**, *14*, 246–256. [[CrossRef](#)]
10. Escudier, M.P.; Gouldson, I.W.; Jones, D.M. Flow of shear-thinning fluids in a concentric annulus. *Exp. Fluids* **1995**, *18*, 225–238. [[CrossRef](#)]
11. Escudier, M.P.; Oliveira, P.J.; Pinho, F.T.; Smith, S. Fully developed laminar flow of non-Newtonian liquids through annuli: Comparison of numerical calculations with experiments. *Exp. Fluids* **2002**, *33*, 101–111. [[CrossRef](#)]
12. Malekmohammadi, S.; Carrasco-Teja, M.; Storey, S.; Frigaard, I.A.; Martinez, D.M. An experimental study of laminar displacement flows in narrow vertical eccentric annuli. *J. Fluid Mech.* **2010**, *649*, 371–398. [[CrossRef](#)]
13. Kim, Y.; Han, S.; Woo, N. Flow of Newtonian and non-Newtonian fluids in a concentric annulus with a rotating inner cylinder. *Korea Aust. Rheol. J.* **2013**, *25*, 77–85. [[CrossRef](#)]
14. Ytrehus, J.D.; Taghipour, A.; Werner, B.; Opedal, N.; Saasen, A. Experimental study of cuttings transport efficiency of water based drilling fluids. In Proceedings of the 33th International Conference on Ocean, Offshore and Arctic Engineering (OMAE2014), San Francisco, CA, USA, 8–13 June 2014; OMAE Paper no. 2014-23960.
15. Ytrehus, J.D.; Taghipour, A.; Sayindla, S.; Lund, B.; Werner, B.; Saasen, A. full scale flow loop experiments of hole cleaning performances of drilling fluids. In Proceedings of the 34th International Conference on Ocean, Offshore and Arctic Engineering (OMAE2015), St. John's, NL, Canada, 31 May–5 June 2015; OMAE Paper no. 2015-41901.
16. Sayindla, S.; Lund, B.; Taghipour, A.; Werner, B.; Saasen, A.; Gyland, K.R.; Ibragimova, Z.; Ytrehus, J.D. Experimental investigation of cuttings transport with oil based drilling fluids. In Proceedings of the 35th International Conference on Ocean, Offshore and Arctic Engineering (OMAE2016), Busan, Korea, 19–24 June 2016; OMAE Paper no. 2016-54047.
17. Bittleston, S.; Ferguson, J.; Frigaard, I.A. Mud removal and cement placement during primary cementing of an oil well-Laminar non-Newtonian displacements in an eccentric annular Hele-Shaw cell. *J. Eng. Math.* **2002**, *43*, 229–253. [[CrossRef](#)]
18. Pelipenko, S.; Frigaard, I.A. On steady state displacements in primary cementing of an oil well. *J. Eng. Math.* **2004**, *46*, 1–26. [[CrossRef](#)]
19. Pelipenko, S.; Frigaard, I.A. Two-dimensional computational simulation of eccentric annular cementing displacements. *IMA J. Appl. Math.* **2004**, *69*, 557–583. [[CrossRef](#)]
20. Pelipenko, S.; Frigaard, I.A. Visco-plastic fluid displacements in near-vertical narrow eccentric annuli: Prediction of travelling-wave solutions and interfacial instability. *J. Fluid Mech.* **2004**, *520*, 343–377. [[CrossRef](#)]
21. Iyoho, A.W.; Azar, J.J. An accurate slot-flow model for non-newtonian fluid flow through eccentric annuli. *Soc. Pet. Eng. J.* **1981**, *21*, 565–572. [[CrossRef](#)]
22. Hele-Shaw, H.S. The flow of water. *Nature* **1898**, *58*, 33–36.
23. Paterson, L. Radial fingering in a Hele Shaw cell. *J. Fluid Mech.* **1981**, *113*, 513–529. [[CrossRef](#)]
24. Thome, H.; Rabaud, M.; Hakim, V.; Couder, Y. The Saffman–Taylor instability: From the linear to the circular geometry. *Phys. Fluids Fluid Dyn.* **1989**, *1*, 224–240. [[CrossRef](#)]
25. Chen, J. Growth of radial viscous fingers in a Hele-Shaw cell. *J. Fluid Mech.* **1989**, *201*, 223–242. [[CrossRef](#)]
26. Cardoso, S.S.S.; Woods, A.W. The formation of drops through viscous instability. *J. Fluid Mech.* **1995**, *289*, 351–378. [[CrossRef](#)]
27. Miranda, J.; Widom, M. Radial fingering in a Hele-Shaw cell: A weakly nonlinear analysis. *Phys. D* **1998**, *120*, 315–328. [[CrossRef](#)]
28. Praud, O.; Swinney, H.L. Fractal dimension and unscreened angles measured for radial viscous fingering. *Phys. Rev. E* **2005**, *72*, 011406. [[CrossRef](#)]
29. Li, S.; Lowengrub, J.; Leo, P.H. A rescaling scheme with application to the long-time simulation of viscous fingering in a Hele–Shaw cell. *J. Comput. Phys.* **2007**, *225*, 554–567. [[CrossRef](#)]
30. Fontana, J.; Dias, E.; Miranda, J. Controlling and minimizing fingering instabilities in non-Newtonian fluids. *Phys. Rev. E* **2014**, *89*, 013016. [[CrossRef](#)]
31. Kondic, L.; Palfy-Muhoray, P.; Shelley, M.J. Models of non-Newtonian Hele-Shaw flow. *Phys. Rev. E* **1996**, *54*, 4536–4539. [[CrossRef](#)] [[PubMed](#)]

32. Kondic, L.; Shelley, M.J.; Palffy-Muhoray, P. Non-Newtonian Hele-Shaw flow and the Saffman-Taylor instability. *Phys. Rev. Lett.* **1998**, *80*, 1433–1436. [[CrossRef](#)]
33. Founargiotakis, K.; Kelessidis, V.C.; Maglione, R. Laminar, transitional and turbulent flow of herschel–bulkley fluids in concentric annulus. *Can. J. Chem. Eng.* **2008**, *86*, 676–683. [[CrossRef](#)]
34. Maleki, A.; Frigaard, I.A. Tracking fluid interfaces in primary cementing of surface casing. *Phys. Fluids* **2018**, *30*, 093104. [[CrossRef](#)]
35. Frigaard, I.A.; Maleki, A. Tracking fluid interface in carbon capture and storage cement placement application. In Proceedings of the 37th International Conference on Ocean, Offshore and Arctic Engineering (OMAE2018), Madrid, Spain, 17–22 June 2018. OMAE Paper no. 2018–77630.
36. Taheri, A.; Ytrehus, J.D.; Taghipour, A.; Lund, B.; Lavrov, A.; Torsæter, M. Use of tracer particles for Tracking fluid interfaces in primary cementing. In Proceedings of the 38th International Conference on Ocean, Offshore and Arctic Engineering (OMAE2019), Glasgow, UK, 9–14 June 2019; OMAE Paper no. 2019–96400.
37. Taheri, A.; Ytrehus, J.D.; Taghipour, A.; Lund, B.; Lavrov, A.; Torsæter, M. Experimental study of the use of particles for tracking the interfaces in primary cementing of concentric and eccentric wells. In Proceedings of the SINTEF Proceedings, Trondheim, Norway, 17–19 June 2019; pp. 91–99.
38. Qwabe, L.; Pare, B.; Jonnalagadda, S.B. Mechanism of oxidation of brilliant cresyl blue with acidic chlorite and hypochlorous acid. A kinetic approach. *S. Afr. J. Chem.* **2005**, *58*, 86–92.